Title

Differential diagnosis of prostate cancer and benign prostatic hyperplasia based on DCE-MRI using bi-directional CLSTM deep learning and radiomics

Journal

Medical & Biological Engineering & Computing, 61(3)

ISSN

0140-0118

Authors

Zhang, Yang

Li, Weikang

Zhang, Zhao

et al.

Publication Date

2023-03-01

DOI

10.1007/s11517-022-02759-x

Peer reviewed

HHS Public Access

Author manuscript

Med Biol Eng Comput. Author manuscript; available in PMC 2023 October 04.

Published in final edited form as:

Med Biol Eng Comput. 2023 March ; 61(3): 757–771. doi:10.1007/s11517-022-02759-x.

Differential diagnosis of prostate cancer and benign prostatic hyperplasia based on DCE-MRI using bi-directional CLSTM deep learning and radiomics

Yang Zhang[1,2], **Weikang Li**[3], **Zhao Zhang**[4], **Yingnan Xue**[4], **Yan-Lin Liu**[2], **Ke Nie**[1], **Min-Ying Su**[2], **Qiong Ye**[5]

[1]Department of Radiation Oncology, Rutgers-Cancer Institute of New Jersey, Robert Wood Johnson Medical School, New Brunswick, NJ, USA

[2]Department of Radiological Sciences, University of California, 164 Irvine Hall, Irvine, CA 92697, USA

[3]Department of Radiology, The Children's Hospital of Zhejiang University School of Medicine, Hangzhou, China

[4]Department of Radiology, The First Affiliated Hospital of Wenzhou Medical University, Wenzhou, China

[5]High Magnetic Field Laboratory, Hefei Institutes of Physical Science, Chinese Academy of Sciences, 350 Shushanhu Road, Hefei 230031, Anhui, People's Republic of China

Abstract

Dynamic contrast-enhanced MRI (DCE-MRI) is routinely included in the prostate MRI protocol for a long time; its role has been questioned. It provides rich spatial and temporal information. However, the contained information cannot be fully extracted in radiologists' visual evaluation. More sophisticated computer algorithms are needed to extract the higher-order information. The purpose of this study was to apply a new deep learning algorithm, the bi-directional convolutional long short-term memory (CLSTM) network, and the radiomics analysis for differential diagnosis of PCa and benign prostatic hyperplasia (BPH). To systematically investigate the optimal amount of peritumoral tissue for improving diagnosis, a total of 9 ROIs were delineated by using 3 different methods. The results showed that bi-directional CLSTM with ± 20% region growing peritumoral ROI achieved the mean AUC of 0.89, better than the mean AUC of 0.84 by using the tumor alone without any peritumoral tissue ($p = 0.25$, not significant). For all 9 ROIs, deep learning had higher AUC than radiomics, but only reaching the significant difference for ± 20%

✉Min-Ying Su, msu@uci.edu; Qiong Ye, 94301699@qq.com.
Qiong Ye and Min-Ying Su contributed equally to this work.

Declarations

This research study was conducted retrospectively. Approval was obtained from the ethics committee of Institutional Review Board and written informed consent was waived. The procedures used in this study adhere to the tenets of the Declaration of Helsinki.

Conflict of interest The authors declare no competing interests.

region growing peritumoral ROI (0.89 vs. 0.79, $p = 0.04$). In conclusion, the kinetic information extracted from DCE-MRI using bi-directional CLSTM may provide helpful supplementary information for diagnosis of PCa.

Keywords

Prostate cancer; Dynamic contrast-enhanced MRI (DCE-MRI); Bi-directional convolutional long short-term memory (CLSTM); Radiomics; Peritumoral

1 Introduction

Prostate cancer (PCa) is one of the most common malignant tumors in men [1]. Patients with PCa and benign conditions such as prostatic hyperplasia and prostatitis can present with similar symptoms and elevated prostate-specific antigen (PSA), which makes diagnosis challenging [2]. The distinction of benign diseases from PCa, and the accurate staging for cancer, is critical for an individual patient to make the optimal management decision [3]. Currently, multi-parametric MRI (mpMRI) is routinely performed for the detection and diagnosis of PCa in the clinic. The protocol typically includes T2-weighted imaging (T2WI), diffusion-weighted imaging (DWI), and dynamic contrast-enhanced MRI (DCE-MRI), exploring both anatomical and functional information of the suspicious tissues in the whole prostate gland and the surrounding pelvic region [4].

Acquired MR images are visually evaluated by radiologists according to the guideline of PI-RADS (Prostate Imaging–Reporting and Data System), and the suspicious lesion is assigned with a risk score. Patients with a PI-RADS v2 score ≥ 3 lesions will be suggested to take a biopsy, which has approximately 70% to be confirmed as PCa by MRI-targeted biopsy [1, 5]. However, even with the standardized reading criteria, the diagnosis of PCa based on MR images may vary considerably, and the agreement for the biopsy decision among experienced radiologists was 78% [5]. In prostate mpMRI protocol, the DWI is considered as the most important sequence, which demonstrates excellent performance in the detection and diagnosis of PCa [6–8]. In the latest version of PI-RADS v2.1, DCE-MRI was degraded as a supplemental sequence [4]. Yet, DCE-MRI can reflect the hemodynamic information related to angiogenesis, which is essential for the growth of cancer. The sequence usually acquires multiple frames of post-contrast images with a high spatial resolution, which contain more information not interpretable by radiologists' visual viewing. More research is needed to fully explore the role of DCE-MRI for diagnosis of PCa.

Artificial intelligence (AI)-based image analysis has been proven as a valuable method to extract quantitative imaging features from the entire lesion and provide information related to tissue heterogeneity to aid in the differentiation of benign and malignant lesions. Several studies have applied AI analysis using deep learning with various convolutional neural network (CNN) and machine learning for diagnosis of PCa [9–11]. However, most of them are based on T2WI and DWI. DCE-MRI acquires a series of images with rich spatial and temporal information, which can only be fully explored by using sophisticated computer algorithms. There are two main AI methods: radiomics with machine learning algorithms

and deep learning using the convolutional neural network. Both methods provide an efficient approach to extract information and train diagnostic models.

It is well known that the peritumoral tissue surrounding the tumor also contains important diagnostic information; however, how much tissue should be included in the analysis has not been systematically investigated. In this study, we used three different methods to extract the peritumoral region: (1) volumetric expansion to 1.2 and 1.5 times; (2) boundary expansion using 5-, 10-, and 15-pixels; and (3) region growing using ± 20%, ± 30%, and ± 40% of the averaged tumor intensity as the stopping criteria. The diagnostic results obtained using the tumor alone and the 8 expanded ROIs with different amounts of peritumoral tissues were compared.

For deep learning, since DCE images contained time information, a recurrent neural network (RNN), convolutional long short-term memory (CLSTM), that could consider the temporal change of input images was applied. For RNN, if the input train was too long, the early information would be discarded due to the use of forget gate; therefore, to solve the problem, we implemented the bi-directional CLSTM to fully utilize the entire set of DCE images. These methods were applied to differentiate between PCa and benign prostatic hyperplasia (BPH).

There are two main objectives in this study: (1) comparison of the diagnostic performance achieved by deep learning and radiomics and (2) comparison of the diagnostic performance of 9 ROIs with different amount of peritumoral tissues. We summarize our contributions as follows. Firstly, we acquired a DCE-MRI dataset with a high spatial and temporal resolution from patients confirmed with PCa and BPH. Secondly, we applied three different methods to define the peritumoral tissues based on volumetric expansion, boundary pixel, and region growing to evaluate and compare their diagnostic performance. Thirdly, we developed a new bi-directional CLSTM as the convolutional neural network to fully utilize the long train of DCE-MRI images for diagnosis. Lastly, we also performed radiomics analysis so the results obtained from the sophisticated deep learning could be compared to the results obtained from the more straightforward radiomics.

2 Materials and methods

2.1 Dataset

A total of 136 patients receiving prostate mpMRI from September 2014 to August 2019 who had confirmed histological diagnosis of PCa and BPH were included in this study. Among them, 74 PCa patients received radical prostatectomy subsequently. A total of 62 BPH patients had identified suspicious lesion with PI-RADS v2 score ≤ 2 and received biopsy within 6 months of MRI. The median prostate-specific antigen (PSA) was 9.80 ng/mL in the PCa group and 6.18 ng/mL in the BPH group, and their median age was 66 and 65 years old, respectively. This is a single-center study, and all datasets were collected at the First Affiliated Hospital of Wenzhou Medical University. The institutional review board approved this retrospective study and waived the requirement for informed consent.

The MR examinations of all patients were carried out on a 3.0 T scanner (Achieve; Philips, The Netherlands) by using the abdominal-phased array sensitivity-encoding (SENSE) torso coil, with the same imaging protocol. Four hours of fasting before MR examination was required to suppress bowel peristalsis. The DCE-MRI protocol was acquired by using the 3D Fast Field Echo (FFE) sequence in the axial direction, with the following parameters: echo time (TE)/repetition time (TR) = 2.4/4.6 ms; flip angle (FA) = 12°; field of view (FOV) = 352 × 264 mm^2; matrix = 320 × 228; slice thickness = 5.0 mm without gap; number of slices = 16; fat suppression = SPAIR; number of average = 1; SENSE = 2.5; temporal resolution = 8.0 s; number of DCE frames = 40; total acquisition time = 5 min 22 s. During the acquisition, the contrast agent (Omniscan, GE) with a dose of 0.1 mmol/kg of body weight was injected via a power injector (Spectris Solaris EP, Samedco Pvt Ltd.) at a flow rate of 2 mL/s, followed by a 20 mL saline flush. The injection was started after 5 pre-contrast frames were acquired. A total of 40 frames were acquired, including 5 pre-contrast (F1–F5) and 35 post-contrast (F6–F40). Only the DCE-MRI images were analyzed in this study. The age, tPSA, PI-RADS v2 scores in the two groups, and ISUP (International Society of Urological Pathology) grades of the diagnosed PCa are listed in Table 1.

2.2 Generation of expanded peritumor ROI

The main objective of this study was to apply deep learning and radiomics to build diagnostic models, by considering different amounts of peritumoral tissues extracted using different methods. The analysis flowchart is shown in Fig. 1. The first task was to segment the lesion ROI, on the subtraction map generated by subtracting averaged pre-contrast images (F1–F5) from the 25th post-contrast image (F25). Two radiologists outlined the index suspicious lesion in consensus on DCE-MRI using ImageJ (NIH, Bethesda, USA). For PCa, the surgical pathological report from the radical prostatectomy was used as the reference for determining the location and the extent of cancer. Figure 2 shows a case example from a PCa patient, demonstrating one pre-contrast and two post-contrast DCE-MRI images acquired at the 15th and 40th frames and the DCE-MRI time course showing the washout pattern. The segmented ROIs on three consecutive slices are shown. For deep learning, a square box is needed as the input, which is generated by projecting all tumor ROIs together, and the smallest bounding box covering the outline of all projected ROIs is illustrated.

The image pre-processing was performed, with main purpose of normalizing the signal intensity acquired during the DCE sequence. First of all, the subtraction images were inspected to determine whether motion correction was needed as a pre-processing step. We did not observe severe motion artifacts in any cases in our dataset, so the motion correction was not necessary. Then, to properly consider the change of signal intensity over time, the selected sets of DCE images were normalized together to a mean = 0 and standard deviation = 1 inside the ROI areas. To reduce the redundant information from the DCE-MRI sequence into the CLSTM network, the length of the image train was reduced from 40 to 25. The 5 pre-contrast frames were averaged as the reference for normalizing post-contrast frames. The early 14 post-contrast DCE-MRI frames that showed a rapid change were included, and the last 20 frames that showed a slow-varying change were down-sampled to 10 frames, by

only selecting every other frame. So, altogether, a total of 25 normalized enhancement maps were used. For all cases, PCa or BPH, the same reduction method was applied.

The peritumoral region was determined by using three different methods with a total of 8 different ROIs. The expanded peritumor region of the Fig. 2 PCa case is shown in Fig. 3. The first method was the volumetric expansion, by enlarging the segmented tumor ROI to 1.2 and 1.5 times. The second method used the boundary pixel expansion by extending the segmented tumor boundary with 5, 10, and 15 pixels. The volumetric and boundary pixel expansion methods were based on the anatomic expansion without considering the intensity information, which can be done by the third method, region growing. First, the mean signal intensity from the entire tumor was calculated from the subtraction map of F25 (the image used for ROI drawing), and the expansion was generated by outward growing used ± 20%, ± 30%, and ± 40% of the mean tumor intensity as the stopping criteria [12]. For example, for ± 20%, the lower stopping criterion was 80% of the mean tumor intensity, and the higher stopping criterion was 120%. For ± 30%, the lower and higher stopping criteria were 70% and 130% of the mean tumor intensity. Figure 4 shows the DCE-MRI images from a patient with confirmed BPH, whose DCE-MRI time course demonstrating the persistent enhancing pattern, and Fig. 5 illustrates the expanded peritumor regions. The manual lesion segmentation was performed using ImageJ (NIH, Bethesda, USA). For the expansion of ROI, it was performed using our own programs written in Matlab (The Mathworks Inc. USA).

2.3 Long short-term memory (LSTM) network

A second module in the flowchart in Fig. 1 is the deep learning using a recurrent neural network (RNN). RNN is a popular model that has been shown great promise in applications involving sequential inputs [13–17], particularly for utilizing temporal information. One issue of the general RNN architecture is the long-term dependencies [18]. This means that the output at any time point can rely on the information from all previous inputs. For the long sequential inputs, the later outputs can gather all of the information from the initial inputs, which works as a crucial feature of RNN [13, 14, 18]. However, during the back-propagation of the training process, after a new input is added into the system, less information can be processed due to the gradients that are difficult to be modified. This is known as “gradient vanishing.” As the gradient is backpropagated to earlier layers, repeated multiplication may make the gradient infinitely small. However, in practice, the present output usually depends on the close context, which means closer inputs and states should be weighted more than others.

LSTM is designed for value-based inputs. All parameters or weights are vectors and the input-to-state and state-to-state transitions are all linear combinations. This is accomplished by the fully connected layers. In our study, the inputs are images [19]. To adjust for this, the fully connected layers are replaced by convolutional layers. Also, the weights become convolutional kernels which reduce the number of parameters and that formulates convolutional long short-term memory (CLSTM). The conceptual workflow of deep learning using the architecture of 7 bi-directional convolutional LSTM layers is shown in Fig. 6. Due to the forget gate implemented in LSTM, information from early time points

contributes less than later time points. To minimize this problem, a bi-directional CLSTM model was applied, as shown in Fig. 7. These implementation details are shown in Fig. 8. H_t and C_t are the temporal hidden states, which are transferred to the cells at the next time point. The 25 selected DCE time frames reduced from the total of 40 frames were used as input. The CLSTM layers consist of 25 cells in each direction, and the whole network is made up of 7 bi-directional CLSTM layers, as shown in Fig. 9.

2.3.1 CLSTM training configurations—The bi-directional CLSTM network was used to train the diagnostic model, by inputting the 25 DCE-MRI images into the network in a time order [18, 19]. Each 2D imaging slice was used as an independent input. The number of the input channel was 1 at each time point. For each case, the smallest bounding box containing the ROI was used as the input, as illustrated in Figs. 2 and 4. The ROIs from all slices were projected together, and the smallest bounding box to cover the outer boundary of projected ROIs was used. The 25 sets of DCE-MRI images were normalized together to a mean = 0 and standard deviation = 1.

For the CLSTM network, 7 stacked CLSTM layers were fed into a final fully connected layer before output. The algorithm was implemented with a standard cross-entropy loss function and the Adam optimizer with an initial learning rate of 0.001, which was kept as a constant throughout the training [20]. The software code was written in Python 3.7 using the open-source TensorFlow 2.0 library (Apache 2.0 license). Experiments were performed on a GPU-optimized workstation with a single NVIDIA GeForce GTX Titan X (12 GB, Maxwell architecture). A forward pass for the classification test of a new patient could be achieved in < 0.01 s. The results were evaluated using fourfold cross-validation by ROC analysis. The range and the mean AUC from the fourfold analyses were calculated to show the diagnostic performance.

2.3.2 Radiomics analysis—The second AI method in the flowchart in Fig. 1 is to perform the radiomics analysis, so the results can be compared to those generated by the deep learning models. The tumor alone and tumor with 8 different peritumoral regions were analyzed. For each case, the ROIs on all slices were combined to generate a 3D mask for extraction of radiomic features by using the PyRadiomics, an open-source radiomics library written in Python [21]. A total of 107 features were extracted on each DCE-MRI image [22], and thus, there were 107 × 40 = 4280 features for each case. For feature reduction, Student's *t*-test was applied to get the corresponding *p*-values between the PCa and BPH groups. Here, we chose a threshold of $p < 0.1$ as a preliminary selection criterion, and only features with *p*-values lower than 0.1 were considered.

This preliminary reduction could reduce the number of features from thousands down to hundreds, and the next step was to select features for differentiation between BPH and PCa. The sequential feature selection process was performed by constructing the multiple support vector machine (SVM) classifiers [23]. The loss function of SVM can be formulated as

$$min_w \parallel w \parallel_2^2 , \; s.t : y_i\left(w^T x_i + b\right) \geq 1$$

where x_i is the ith inputs and y_i is the ith corresponding label. w is the trainable weights and b is the bias. To penalize the misclassified cases, we can apply the hinge function to reformat the loss function as

$$min_w \parallel w \parallel_2^2 + \lambda \sum_i hinge\left(y_i\left(w^T x_i\right)\right)$$

where the hinge function is

$$hinge(z) = \max\{0, 1 - z\}$$

The hinge function is a convex function. Then, the loss function can be solved by using the gradient descent algorithms.

For feature selection, we used the SVM with Gaussian kernel as the objective function to test the performance of models built with a subset of features [24, 25]. The methods were implemented using our own programs written in Matlab. In the beginning, an empty candidate set was presented, and features were sequentially added. The fourfold cross-validation method was applied to test the model performance [26]. The split of the training and validation subsets was assigned before the feature selection process. Only features extracted from cases in the training dataset were considered to build the model, and then, the developed model was applied to the set-aside cases in the validation dataset. In each iteration, the training process was repeated 1000 times to explore the robustness of each feature. After each iteration, the feature which led to the best performance was added to the candidate set. When the addition of a new feature did not meet the criterion, the selection process stopped. Here, we used 10^{-6} as termination tolerance for the objective function value. In each test, the originally selected features were larger than 20, which was too many considering the small number of cases. Based on the selection results, the discriminating capability of features could be assessed and ranked. According to the ranking, the top 1, 2, 3, 4, 5, … 20 features were selected, and they were used to build the diagnostic model by adding them one by one. The discrimination accuracy was evaluated by ROC. We found that by increasing the number of features from 1 to 4, the accuracy improved substantially, and when adding more features from 4 to 6, the accuracy improved slightly. When adding more features beyond 6, the accuracy did not increase further. Therefore, finally 6 features were selected to build the classification model.

After the feature selection was completed, the 6 selected features were used to train the SVM model with Gaussian kernel to serve as the final diagnostic classifier. The diagnostic performance was evaluated using fourfold cross-validation, i.e., the model developed using 75% cases was tested in the remaining 25% cases, balanced between PCa and BPH cases. The predicted radiomic scores from cases in the testing dataset were used to construct the ROC curve, and the AUC was calculated. The range of AUC from the 4 runs of validation tests and the mean AUC was obtained. Each case had only one chance to be included in the testing dataset, and the obtained radiomics scores from all cases were combined to build a final ROC.

2.3.3 Statistical analysis—The DeLong test was applied to compare the ROC curves generated using the deep learning and the radiomics analysis. For the comparison of different ROIs, the best performance ROI was used as the reference to check whether the result of other ROI was significantly worse. $p < 0.05$ was considered significant.

3 Results

3.1 ROC analysis of deep learning using bi-directional CLSTM

The diagnostic results using 9 ROIs as the input into the bi-directional CLSTM are summarized in Table 2. For the tumor alone without any peritumoral tissue, the range of AUC in the fourfold cross-validation was 0.72–0.89 (mean 0.84). When using the expanded ROI as input, in general, adding a small amount of peritumoral tissue achieved a higher AUC compared to using tumor alone. When using the 1.2 times volumetric expansion, the mean AUC = 0.85; when using the 5-pixel boundary expansion, the mean AUC = 0.87; and when using the ± 20% region growing, it had the highest mean AUC of 0.89 [range 0.81–0.93]. For each expansion method, the AUC decreased with the enlarged ROI. When going from 1.2 to 1.5 times volumetric expansion, the mean AUC decreased from 0.85 to 0.75. With the increasing boundary expansion using 5, 10, and 15 pixels, the mean AUC decreased from 0.87 to 0.85 to 0.74. In the region growing using ± 20%, ± 30%, and ± 40% stopping criteria, the mean AUC decreased from 0.89 to 0.77 to 0.65. The DeLong test results using the 20% region growing ROI as the reference are shown in Table 3. The p value compared with the lesion-only ROI was 0.25, not significantly different. The difference compared with the ROI generated using 1.2 times shell; 5- and 10-pixel expansions were also not significant.

3.2 Diagnostic results of radiomics analysis

The radiomics diagnostic results are also summarized in Table 2, and the DeLong comparison z and p values between radiomics and deep learning are listed in the table. The range and mean AUC obtained from fourfold cross-validation are listed for all 9 ROIs. The mean AUC for the tumor alone was 0.77 [range 0.70–0.82]. Including peritumoral tissue generated with ± 20% region growing had the best performance, with a mean AUC of 0.79 [range 0.74–0.85], not significantly different, $p = 0.72$ by the DeLong test. For the radiomics analysis, there were 6 features selected by SVM. Their box plots between the PCa and BPH groups are shown in Fig. 10. The calculated radiomics score between the two groups, which represents the malignancy probability, is shown in Fig. 11. The results for the expanded ROI were also consistent with those obtained from deep learning, showing worse AUC with more inclusion of peritumoral tissues. When going from 1.2 to 1.5 times volumetric expansion, the mean AUC decreased from 0.77 to 0.74. When using 5-, 10-, and 15-pixel expansions, the AUC were 0.78, 0.78, and 0.69, respectively. In the region growing with ± 20%, ± 30%, and ± 40% stopping criteria, similarly, as the peritumoral areas expanded larger the performance became worse, showing decreased AUC from 0.79 to 0.72 to 0.62. The DeLong test results using the 20% region growing ROI as the reference are shown in Table 4. The values of the mean AUC were close, and most comparisons did not reach the significant level.

The ROC curves of the tumor alone and the tumor with ± 20% region growing peritumor are shown in Fig. 12. It shows that deep learning has a higher AUC than radiomics and that including peritumoral tissue using ± 20% region growing has a better yet non-significant performance than tumor alone ROI.

4 Discussion

In this study, we demonstrated that the recurrent neural network using bi-directional CLSTM could consider the change of signal intensity in the DCE-MRI series, and reached the highest AUC of 0.89 [range 0.81–0.93] in differentiating PCa and BPH. We performed a systematic analysis comparing 9 different ROIs with different amounts of peritumoral tissue outside the lesion. When using the ± 20% region growing to determine the expansion according to the tumor enhancement intensity, the diagnostic performance was the best. Compared to using tumor alone, the mean AUC was improved from 0.84 to 0.89, but did not reach the significance level. For radiomics analysis, the best model was also obtained when using the 20% region growing ROI, with a mean AUC of 0.79 [range 0.74–0.85]. Overall, the performance of deep learning models was better than the radiomics models, yet only 20% region growing ROI reached a significant difference ($p = 0.04$).

Radiomics and deep learning have been widely applied in the diagnosis and risk stratification of PCa [27–29] and also used in personalized radiation therapy planning to achieve precise treatment [30]. Utilization of texture analysis based on T2WI and apparent diffusion coefficient (ADC) maps for the diagnosis of PI-RADS 3 lesions was evaluated, and yielded an AUC range of 0.775–0.821 for the categorization of prostate cancer (GS ≥ 6) versus no cancer [31]. The diagnostic performance is known to vary with the employed feature selection and machine learning algorithms [32].

For prostate multi-parametric MRI, diffusion-weighted imaging (DWI) is known to be the most important sequence. PCa is characterized by restricted molecular diffusion partially due to increased cell density, so DWI is widely used for the detection and diagnosis of PCa. Liu et al. applied intravoxel incoherent motion DWI (IVIM) to differentiate PCa from BPH, showing the highest AUC of 0.93 [33]. Shao et al. improved the PCa and BPH classification using the three-player minimax game framework and achieved an AUC of 93.4% [34]. However, diffusion MRI commonly suffers from relatively low spatial resolution, which might hamper the detection of small lesions.

DCE-MRI is commonly considered by radiologists using qualitative or semi-quantitative assessment. Since angiogenesis and increased perfusion can happen in both PCa and BPH, previous studies reported inconsistent results in terms of the contribution of DCE-MRI to the diagnosis of PCa. Because the normal prostate gland also showed enhancement, the diagnosis of PCa and BPH could not be made based on one, or a few, contrast-enhanced images. The pattern of the DCE-MRI kinetics (or, the signal intensity time curve) was needed. In our protocol, we had a total of 40 sets of DCE-MRI images with a very fine temporal resolution of 8 s, and this sequence could provide more information compared to the typical DCE-MRI included in the clinical prostate mpMRI protocol.

The deep learning was performed using a long short-term memory (LSTM) network, one of the recurrent neural network (RNN) that can connect previous information to the present task. The LSTM is explicitly designed to avoid long-term dependency and focus primarily on short-term memory. The algorithm can consider the change of signal intensity on the images acquired at different DCE-MRI time points and thus was employed in this study. As illustrated in the case example, the PCa showed the washout DCE-MRI kinetic pattern while the BPH showed the persistent enhancing DCE-MRI kinetic pattern, and the information could only be utilized when the full spectrum of DCE-MRI images was considered. The same hierarchical features were calculated from each timeframe, and the collected information from all DCE-MRI frames was used for classification. The forget gate implemented in LSTM is designed to eliminate old information from the earlier time points. To preserve the information from the entire time series, we employed two methods: firstly to shorten the image train from 40 to 25 and secondly to combine CLSTM from 2 directions by implementing the bi-directional CLSTM. The results showed that this deep learning strategy could achieve a higher accuracy compared with radiomics.

Several studies have also applied deep learning algorithms for diagnosis of PCa [9–11]. In [9], Le et al. applied a multimodal CNN combined with the results based on handcrafted features using a support vector machine (SVM) classifier to diagnose PCa. The T2WI and ADC from 364 patients with a total of 463 PCa lesions and 450 identified noncancerous image patches were analyzed. In our study, differentiation of PCa vs. BPH was a much more challenging task than the differentiation of PCa vs. non-cancer prostate gland. Zhu et al. [10] implemented a stacked auto-encoder (SAE) to extract high-level features to build a random forest model to differentiate PCa and BPH using T2WI, DWI, and ADC. This was a pilot feasibility study, tested on 21 patients. Yuan et al. [11] established a transfer learning model based on ALexNet, which was pre-trained using natural images. The axial T2WI, sagittal T2WI, and apparent diffusion coefficient (ADC) from 132 cases were used to fine-tune the network. The features extracted from AlexNet were used to predict the malignancy probabilities. In the present study, we applied RNN to analyze DCE-MRI for differential diagnosis of PCa and BPH, which has not been reported in the literature so no results to be compared to.

Another major objective of this study was to systematically investigate the contribution of peritumoral tissue for diagnosis. Since altered vasculature is not confined to malignant tissue but infiltrates into the vicinity of the tumor, peritumoral tissue may contain useful diagnostic information [35]. It has been shown that adding perilesional radiomic features to intralesional features could improve discrimination ability in the diagnosis of PCa [36]. Furthermore, including peritumoral tissue outside the tumor ROI may reduce the uncertainties in the lesion ROI drawing. However, how much tissue should be included needs to be carefully determined. As shown in our results, including a small amount of peritumoral tissue could improve accuracy, but when the ROI was expanding too much, the lesion information might be diluted by including the weakly enhanced surrounding tissues and decreased the diagnostic accuracy. The DeLong test showed that there was no significant difference between lesion alone, ROI with small amount of peritumoral tissues (1.2 times shell, 5- and 10-pixel expansion), compared to the best performing ROI with 20% regional

growing. The results suggest that the drawing of lesion ROI does not need to be precise, which may help the clinical implementation of the developed methods for diagnosis.

Ultrasound is routinely used in the systematic biopsy of the prostate for patients presenting with elevated PSA. Similar to DCE-MRI, a new technique, dynamic contrast-enhanced ultrasound imaging (DCE-US) has been applied to quantitatively explore the vascular characterization of the prostate gland with the aid of an intravenously administrated US contrast agent. By using the 3D whole-mount histopathology as the reference, a pixel-wise AUC of 0.72–0.80 was obtained for the detection of PCa [37]. Also, to fully utilize all DCE-US information, the long short-term memory (LSTM) network was applied and demonstrated excellent performance in separating cancer from benign tissue with the highest AUC of 0.96 [38]. Another study adopted the quantitative information of the heterogeneity of flow derived from DCE-US and yielded an AUC of 0.85 for the detection of PCa [39]. However, since the analyzed patient series were different, it was difficult to compare diagnostic results reported in the literature.

There are several limitations in our study. Firstly, the sample size is relatively small. Improved differential performance is expected with a larger sample size. Secondly, all cases are from a single institute, which might hamper the versatility of our prediction model. Thirdly, automatic delineation of index lesion might avoid personal bias in the ROI delineation. Cao et al. used a novel multi-class CNN, FocalNet, to detect the PCa lesion and achieved 89.7% sensitivity for the index lesion [40]. Lastly, we only focused the analysis only on DCE-MRI. Some of patients included in this study also had high-quality T2WI and DWI, and the results for stratifying the risk based on the Gleason Score have been reported before. Li et al. [41] showed that the combination of DWI and hemodynamic information derived from DCE-MRI could stratify risk of PCa in the central gland. Chen et al. [7] also showed that DWI could differentiate International Society of Urological Pathology (ISUP) Gleason Grade (GG) ≤ 2 vs. ≥ 3 groups for the peripheral zone PCa. Zhang et al. [8]. showed that the combination of whole-lesion ADC and PSA could differentiate between low-grade (Gleason score [GS] ≤ 6) and high-grade (GS ≥ 7) PCa.

In conclusion, this study demonstrates that deep learning using the bi-directional CLSTM network, with appropriate consideration of the peritumoral information, can be implemented to analyze the DCE-MRI for differentiation of PCa and BPH. The results obtained using 9 different ROIs showed that including a small amount of peritumoral tissue, such as using anatomic expansion to 1.2 times volume, 5-, 10-pixel outward boundary, or using enhancement intensity expansion with ± 20% regional growing, could improve diagnostic performance compared to using the tumor ROI alone. Even the improvement did not reach the significant level, the results suggest that drawing of lesion ROI does not need to be precise and that including small amount of peritumoral tissue will help in diagnosis. Our results were consistent with the current recommendation that DCE-MRI may provide supplementary information. For patients presenting with elevated PSA or symptoms, correct diagnosis of PCa and BPH, and further risk stratification of PCa, is vital for making optimal personalized treatment decisions. Deep learning may provide a feasible strategy to fully explore all information contained in a large number of MR images acquired in a prostate mpMRI protocol.

Biographies

Dr. Yang Zhang is currently a medical physics resident at Rutgers—Robert Wood Johnson University Hospital. He obtained his PhD in Biomedical Engineering from University of California Irvine and participated in several high-profile conferences. His research interests lie in the area of medical image processing and machine learning.

Mr. Weikang Li received the M.S. degree in Biomedical Engineering from Wenzhou Medical University, Wenzhou, China, in 2021. Research Interests: Investigate the application of deep learning in medical imaging.

M.D. Zhao Zhang received his M.S. degree in Zhejiang University, China. Mr. Zhao Zhang is a radiologist at The First Affiliated Hospital of Wenzhou Medical University, Wenzhou, Zhejiang, China.

M.D. Yingnan Xue received the B.S. degree in Medical Imageology from China Medical University, Shenyang, China, in 2009 and the M.S. degree in Imaging and Nuclear Medicine from Wenzhou Medical University, Wenzhou, China, in 2020. Research Interests: Investigate the application value of multiparametric magnetic resonance imaging predicts biochemical recurrence after surgery for prostate cancer.

Dr. Yan-Lin, Liu received his Ph.D. in Nuclear Engineering from National Tsing Hua University. He is currently working on Deep learning for medical imaging and analysis at University of California Irvine.

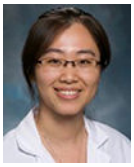

Dr. Ke Nie received the B.S. degree from the University of Science and Technology of China, Hefei, China, and the Ph.D. degree from the University of California, Irvine. She is currently an Associate Professor at Rutgers University, NY, USA. Her research interests include general radiological physics, IGRT, image registration, perfusion CT, and radiomics. Dr. Nie is the Director of the Medical Physics Residency Program and the Director of GammaKnife Physics at the Robert Wood Johnson Medical School, Rutgers University.

Dr. Min-Ying Su is a professor of Radiological Sciences and the director of the Tu & Yuan Center for Functional Onco-Imaging at the University of California, Irvine, working on AI-based imaging analysis for clinical applications.

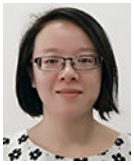

Dr. Qiong Ye is an associate Scientist at High Magnetic Field Laboratory, Hefei Institutes of Physical Science, Chinese Academy of Sciences. She is currently working on both clinical and preclinical advanced magnetic resonance imaging and spectroscopy.

References

1. Siegel RL, Miller KD, Jemal A (2018) Cancer Statistics, 2018. CA Cancer J Clin 68(1):7–30. 10.3322/caac.21442 [PubMed: 29313949]
2. Weinreb JC et al. (2016) PI-RADS prostate imaging–reporting and data system: 2015, version 2. Eur Urol 69(1):16–40 [PubMed: 26427566]

3. Herold CJ et al. (2016) Imaging in the age of precision medicine: summary of the proceedings of the 10th Biannual Symposium of the International Society for Strategic Studies in Radiology. Radiology 279(1):226–238 [PubMed: 26465058]
4. Turkbey B et al. (2019) Prostate Imaging Reporting and Data System Version 2.1: 2019 Update of Prostate Imaging Reporting and Data System Version 2. Eur Urol. 10.1016/j.eururo.2019.02.033
5. Kasivisvanathan V et al. (2018) MRI-targeted or standard biopsy for prostate-cancer diagnosis. N Engl J Med 378(19):1767–1777. 10.1056/NEJMoa1801993 [PubMed: 29552975]
6. Hectors SJ et al. (2018) Advanced diffusion-weighted imaging modeling for prostate cancer characterization: correlation with quantitative histopathologic tumor tissue composition-a hypothesis-generating study. Radiology 286(3):938–948. 10.1148/radiol.2017170904 [PubMed: 29091749]
7. Chen Z et al. (2020) The performance of intravoxel-incoherent motion diffusion-weighted imaging derived hypoxia for the risk stratification of prostate cancer in peripheral zone. Eur J Radiol 125:108865. 10.1016/j.ejrad.2020.108865 [PubMed: 32058895]
8. Zhang Z et al. (2019) Risk stratification of prostate cancer using the combination of histogram analysis of apparent diffusion coefficient across tumor diffusion volume and clinical information: a pilot study. J Magn Reson Imaging 49(2):556–564. 10.1002/jmri.26235 [PubMed: 30173421]
9. Le MH et al. (2017) Automated diagnosis of prostate cancer in multi-parametric MRI based on multimodal convolutional neural networks. Phys Med Biol 62(16):6497 [PubMed: 28582269]
10. Zhu Y et al. (2017) MRI-based prostate cancer detection with high-level representation and hierarchical classification. Med Phys 44(3):1028–1039 [PubMed: 28107548]
11. Yuan Y et al. (2019) Prostate cancer classification with multiparametric MRI transfer learning model. Med Phys 46(2):756–765 [PubMed: 30597561]
12. Forsyth DA, Ponce J (2002) Computer vision: a modern approach. Prentice Hall Professional Technical Reference, Hoboken
13. Bengio Y (2009) Learning deep architectures for AI. Foundations and trends® in Machine Learning 2(1):1–127. 10.1561/2200000006
14. Goodfellow I, Bengio Y, Courville A (2017) Deep learning (vol 1). MIT press, Cambridge
15. LeCun Y, Bengio Y, Hinton G (2015) Deep learning. Nature 521(7553):436–444. 10.1038/nature14539 [PubMed: 26017442]
16. Lee J-G et al. (2017) Deep learning in medical imaging: general overview. Korean J Radiol 18(4):570–584. 10.3348/kjr.2017.18.4.570 [PubMed: 28670152]
17. Schmidhuber J (2015) Deep learning in neural networks: an overview. Neural Netw 61:85–117 [PubMed: 25462637]
18. Hochreiter S, Schmidhuber J (1997) Long short-term memory. Neural Comput 9(8):1735–1780 [PubMed: 9377276]
19. Xingjian S et al. (2015) Convolutional LSTM network: a machine learning approach for precipitation nowcasting. Adv Neural Inf Process 28:802–210 10.5555/2969239.2969329
20. Kingma D, Ba J (2014) Adam: a method for stochastic optimization. arXiv preprint arXiv:1412.6980
21. Van Griethuysen JJ et al. (2017) Computational radiomics system to decode the radiographic phenotype. Can Res 77(21):e104–e107
22. Haralick RM, Shanmugam K (1973) Textural features for image classification. IEEE Trans Syst Man Cybern 6:610–621
23. Guyon I, Elisseeff A (2003) An introduction to variable and feature selection. J Mach Learn Res 3 Mars:1157–1182
24. Drucker H et al. (1996) Support vector regression machines. Adv Neural Inf Process Syst 9:155–161. 10.5555/2998981.2999003
25. Tong S, Chang E (2001) Support vector machine active learning for image retrieval. In Proceedings of the ninth ACM international conference on Multimedia. ACM
26. Hastie T, Tibshirani R, Friedman J (2009) The elements of statistical learning: data mining, inference, and prediction, 2nd edn. Springer, New York

27. Brancato V et al. (2021) Evaluation of a multiparametric MRI radiomic-based approach for stratification of equivocal PI-RADS 3 and upgraded PI-RADS 4 prostatic lesions. Sci Rep 11(1):643. 10.1038/s41598-020-80749-5 [PubMed: 33436929]
28. Li M et al. (2020) Radiomics prediction model for the improved diagnosis of clinically significant prostate cancer on biparametric MRI. Quant Imaging Med Surg 10(2):368–379. 10.21037/qims.2019.12.06 [PubMed: 32190563]
29. Cuocolo R et al. (2019) Machine learning applications in prostate cancer magnetic resonance imaging. Eur Radiol Exp 3(1):35. 10.1186/s41747-019-0109-2 [PubMed: 31392526]
30. Leech M et al. (2021) Mini review: personalization of the radiation therapy management of prostate cancer using MRI-based radiomics. Cancer Lett 498:210–216. 10.1016/j.canlet.2020.10.033 [PubMed: 33160001]
31. Giambelluca D et al. (2021) PI-RADS 3 lesions: role of prostate MRI texture analysis in the identification of prostate cancer. Curr Probl Diagn Radiol 50(2):175–185. 10.1067/j.cpradiol.2019.10.009 [PubMed: 31761413]
32. Bernatz S et al. (2020) Comparison of machine learning algorithms to predict clinically significant prostate cancer of the peripheral zone with multiparametric MRI using clinical assessment categories and radiomic features. Eur Radiol 30(12):6757–6769. 10.1007/s00330-020-07064-5 [PubMed: 32676784]
33. Liu X et al. (2013) Biexponential apparent diffusion coefficients values in the prostate: comparison among normal tissue, prostate cancer, benign prostatic hyperplasia and prostatitis. Korean J Radiol 14(2):222–232. 10.3348/kjr.2013.14.2.222 [PubMed: 23483254]
34. Shao Y et al. (2020) Improving prostate cancer (PCa) classification performance by using three-player minimax game to reduce data source heterogeneity. IEEE Trans Med Imaging 39(10):3148–3158. 10.1109/tmi.2020.2988198 [PubMed: 32305907]
35. Rubin MA et al. (1999) Microvessel density in prostate cancer: lack of correlation with tumor grade, pathologic stage, and clinical outcome. Urology 53(3):542–547 [PubMed: 10096381]
36. Zhang H et al. (2021) Diagnostic nomogram based on intralesional and perilesional radiomics features and clinical factors of clinically significant prostate cancer. J Magn Reson Imaging 53(5):1550–1558. 10.1002/jmri.27486 [PubMed: 33851471]
37. Wildeboer RR et al. (2018) Convective-dispersion modeling in 3D contrast-ultrasound imaging for the localization of prostate cancer. IEEE Trans Med Imaging 37(12):2593–2602. 10.1109/tmi.2018.2843396 [PubMed: 29993539]
38. Azizi S et al. (2018) Deep recurrent neural networks for prostate cancer detection: analysis of temporal enhanced ultrasound. IEEE Trans Med Imaging 37(12):2695–2703. 10.1109/tmi.2018.2849959 [PubMed: 29994471]
39. van Sloun RJG et al. (2017) Entropy of ultrasound-contrast-agent velocity fields for angiogenesis imaging in prostate cancer. IEEE Trans Med Imaging 36(3):826–837. 10.1109/tmi.2016.2629851 [PubMed: 28113929]
40. Cao R et al. (2019) Joint prostate cancer detection and Gleason Score prediction in mp-MRI via FocalNet. IEEE Trans Med Imaging 38(11):2496–2506. 10.1109/tmi.2019.2901928 [PubMed: 30835218]
41. Li J et al. (2018) Support vector machines (SVM) classification of prostate cancer Gleason score in central gland using multiparametric magnetic resonance images: A cross-validated study. Eur J Radiol 98:61–67. 10.1016/j.ejrad.2017.11.001 [PubMed: 29279171]

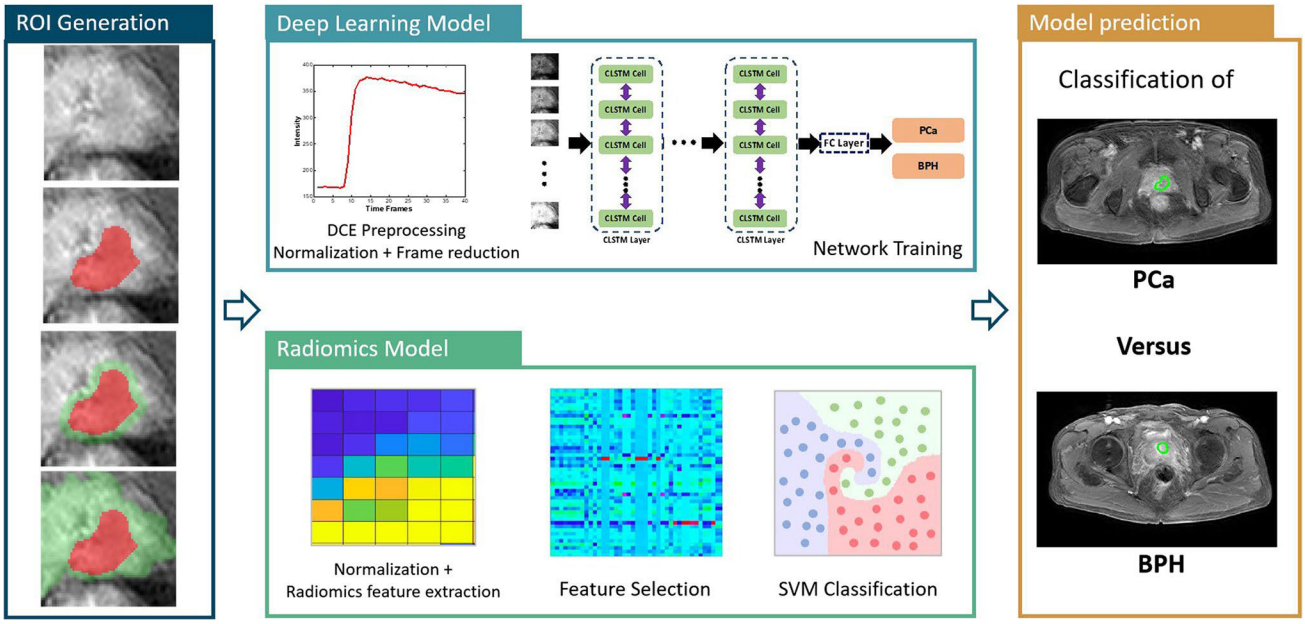

Fig. 1.

The overall analysis flowchart. The first task is to segment the lesion ROI and generate 8 different peritumor regions. The second module is to perform two AI-based analyses, using deep learning with the bi-directional CLSTM network (top), and the radiomics to extract features and perform feature selection and classification with the SVM (bottom). The third module is to obtain the diagnostic results using the developed models to differentiate between PCa and BPH for comparison

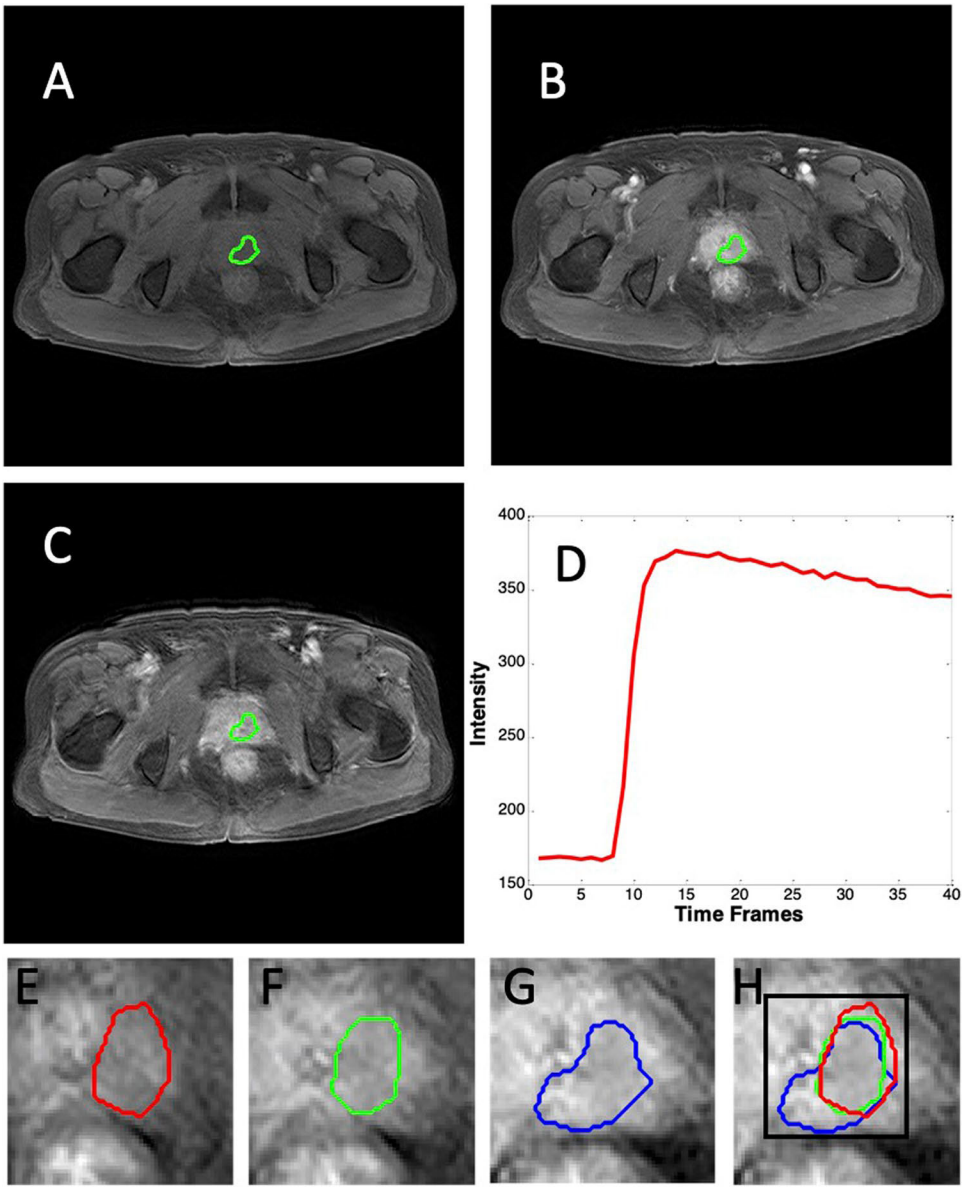

Fig. 2.

A case example of an 83-year-old man with prostate cancer (tPSA = 7.13 ng/mL, Gleason Score = 4 + 5). The suspicious lesion is manually outlined. **A** The first DCE-MRI time frame (pre-contrast image); **B** the 15th time frame post-contrast image; **C** the 40th time frame post-contrast image; **D** the DCE-MRI time-intensity curve shows the washout pattern. **E**, **F**, **G** The tumor ROIs drawn on 3 consecutive slices; **H** the projection of 3 tumor ROIs, and the square smallest bounding box to cover the outer boundary

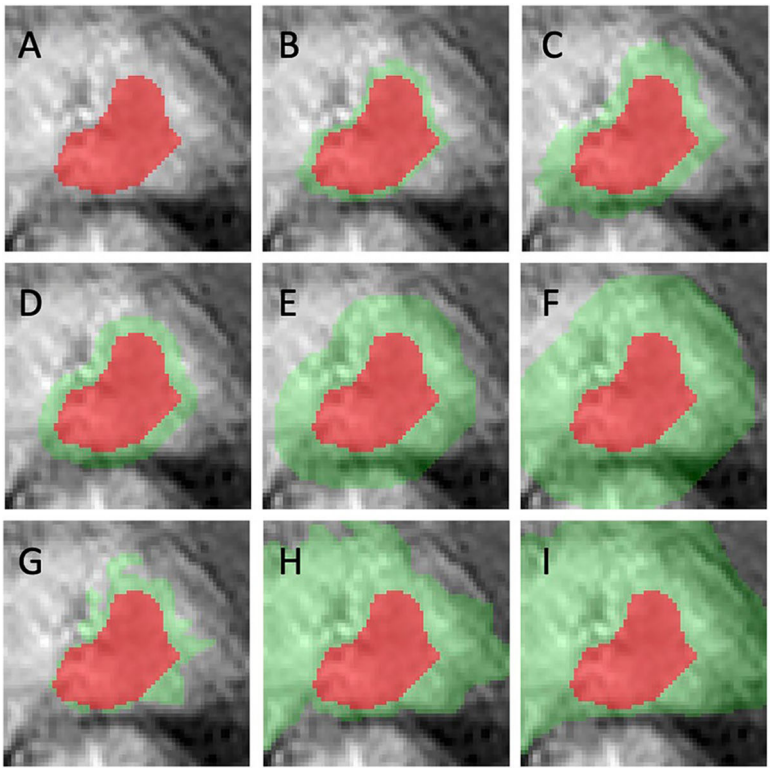

Fig. 3.

Nine different ROIs used in the diagnostic evaluation for the PCa case shown in Fig. 2, generated by using three different methods. **A** Original tumor ROI by manual drawing; **B**, **C** the 1.2 and 1.5 times volumetric expansion; **D**, **E**, **F** the boundary pixel expansion using 5, 10, and 15 pixels; **G**, **H**, **I** the region growing using ± 20%, ± 30%, and ± 40% mean tumor intensity as the stopping criteria

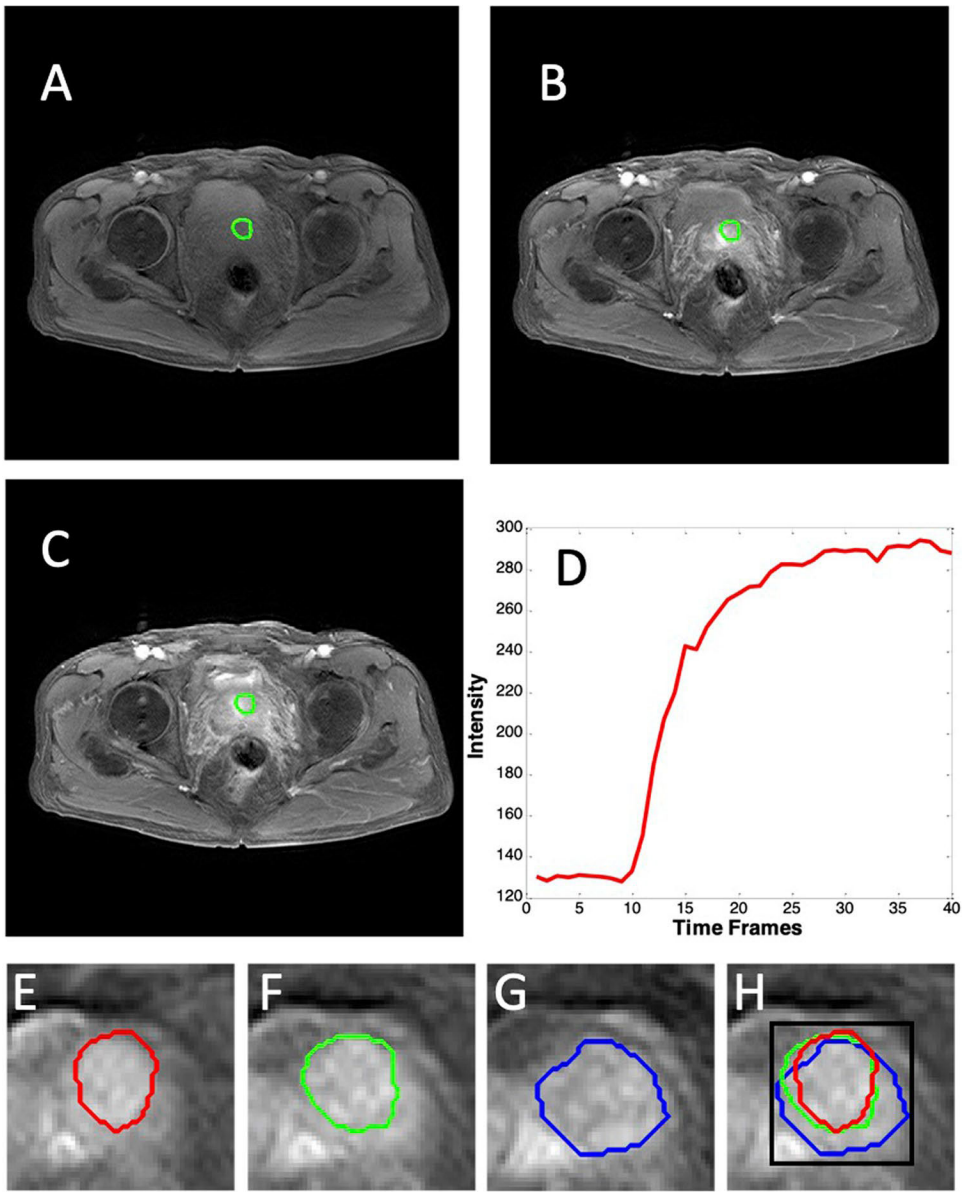

Fig. 4.

A case example of a 72-year-old man with benign prostatic hyperplasia (tPSA = 10.8 ng/mL). The suspicious lesion is manually outlined. **A** The first DCE-MRI time frame (pre-contrast image); **B** the 15th time frame post-contrast image; **C** the 40th time frame post-contrast image; **D** the DCE-MRI time-intensity curve shows the persistent enhancing pattern. **E**, **F**, **G** The tumor ROIs drawn on 3 consecutive slices; **H** the projection of 3 tumor ROIs, and the square smallest bounding box to cover the outer boundary

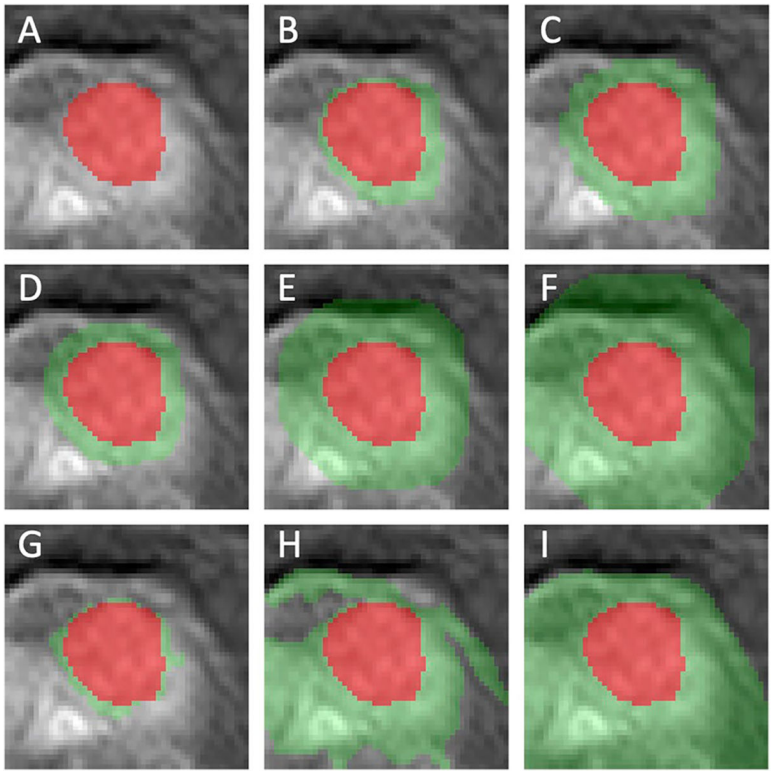

Fig. 5.

Nine different ROIs used in the diagnostic evaluation for the BPH case shown in Fig. 4, generated by using three different methods. **A** Original tumor ROI by manual drawing; **B**, **C** the 1.2 and 1.5 times volumetric expansion; **D**, **E**, **F** the boundary pixel expansion using 5, 10, and 15 pixels; **G**, **H**, **I** the region growing using ± 20%, ± 30%, and ± 40% mean tumor intensity as the stopping criteria

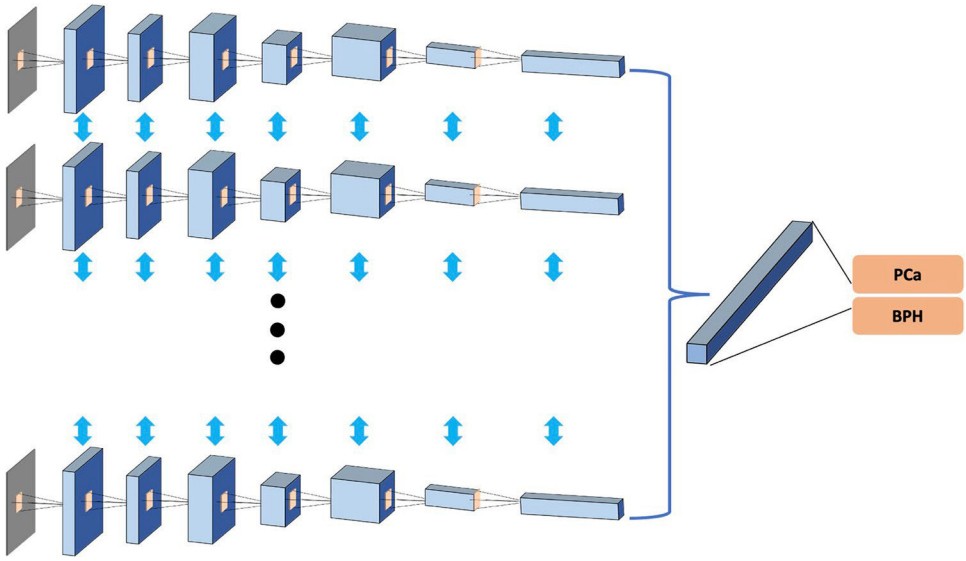

Fig. 6.

Conceptual diagram of the bi-directional convolutional long short-term memory (CLSTM) architecture. The architecture uses 7 convolutional LSTM layers via 3 × 3 filters. The number of DCE-MRI time points is 25. The number of the input channels is 1 at each time point. The number of activation channels in deeper layers is progressively increased from 8 to 16 to 32 to 64. The last dense layer is obtained by flattening the convolutional output feature maps from all states

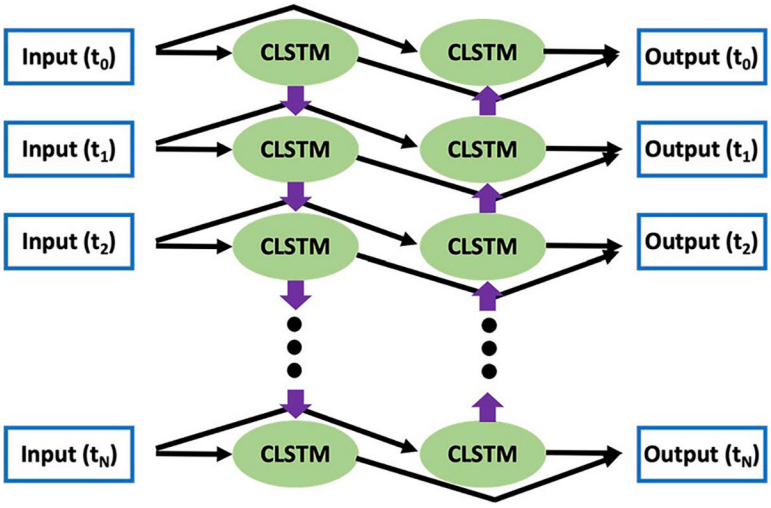

Fig. 7.

Diagram of a bi-directional CLSTM layer. One bi-directional layer is made up of 2 sublayers from opposite directions. The two sublayers have the same inputs, with reversed time orders. The outputs of the 2 sublayers are concatenated together as different channels

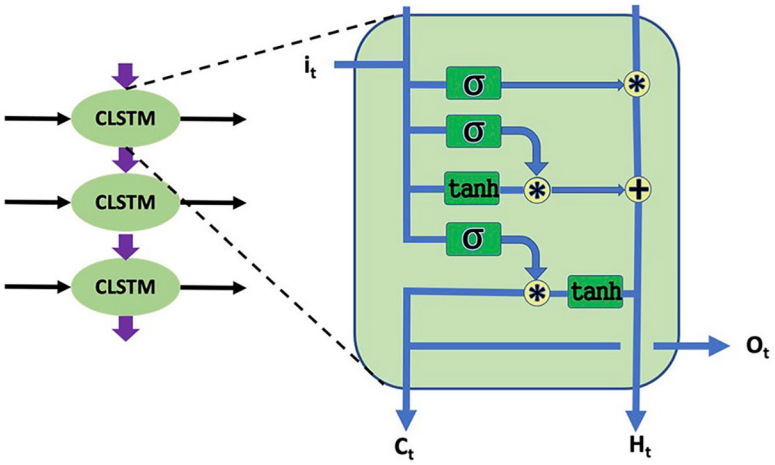

Fig. 8.

Diagram of the CLSTM cell. i_t and o_t are the input and output at time point t. C_t and H_t represent the hidden states which are transferred to the cells on the next time points

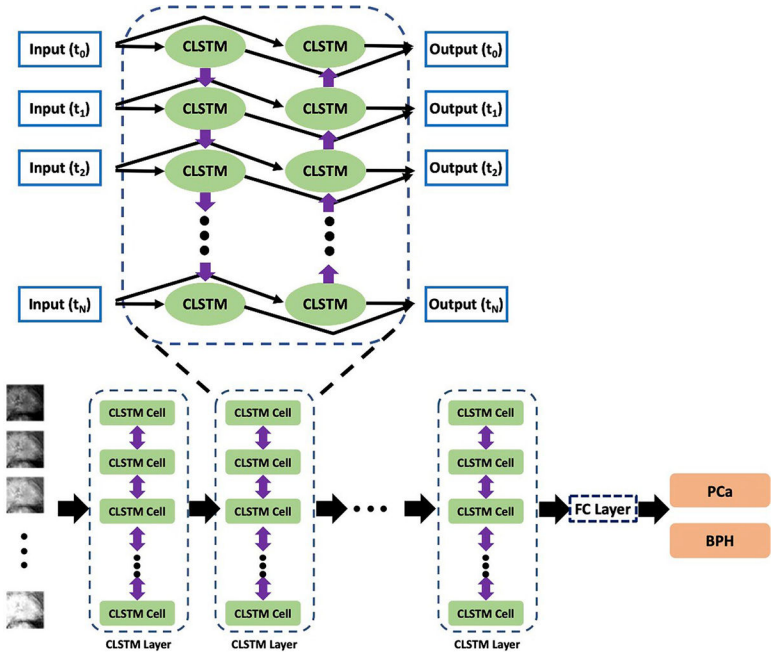

Fig. 9.

The integrated architecture of the bi-directional CLSTM network. Each layer contains the bi-directional LSTM module as shown in Fig. 7. The 25 sets of DCE-MRI images are used as input. After 7 bi-directional LSTM layers, the last dense layer is obtained by flattening the convolutional output feature maps from all states

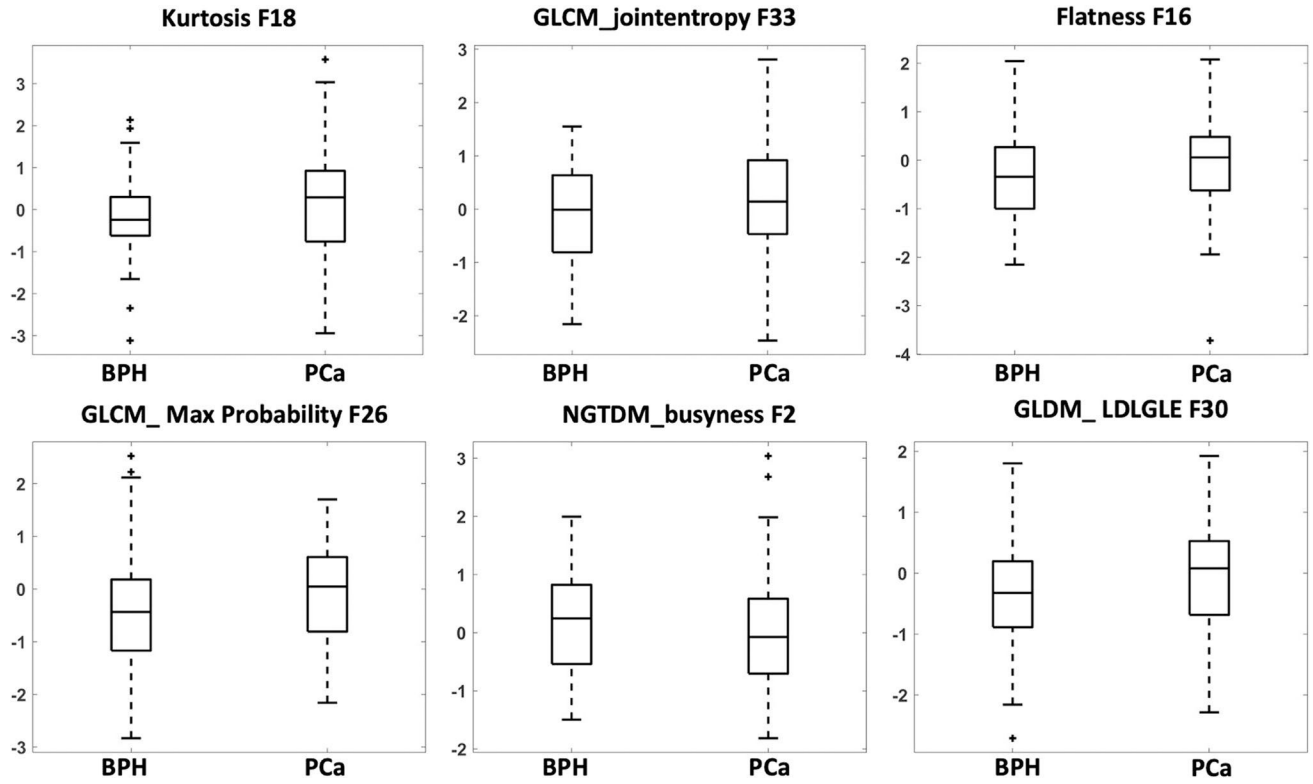

Fig. 10.

The box plot of 6 radiomics features selected by the SVM for diagnosis, by using the ROI of the tumor with ± 20% region growing peritumor tissue. The selected features are from different DCE-MRI frames, including F2, F16, F18, F26, F30, and F33

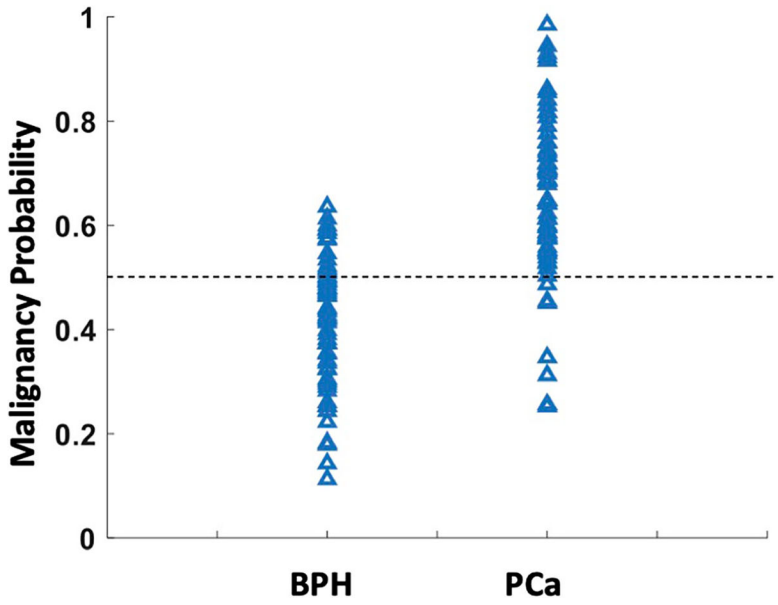

Fig. 11.

The malignancy probability (the radiomics score) calculated by using the model built using the 6 selected features extracted from the tumor with 20% region growing peritumor tissue, shown in Fig. 10. Using the threshold of ≥ 0.5 as malignant, the overall accuracy is 83%, with the sensitivity of 90% and specificity of 73%

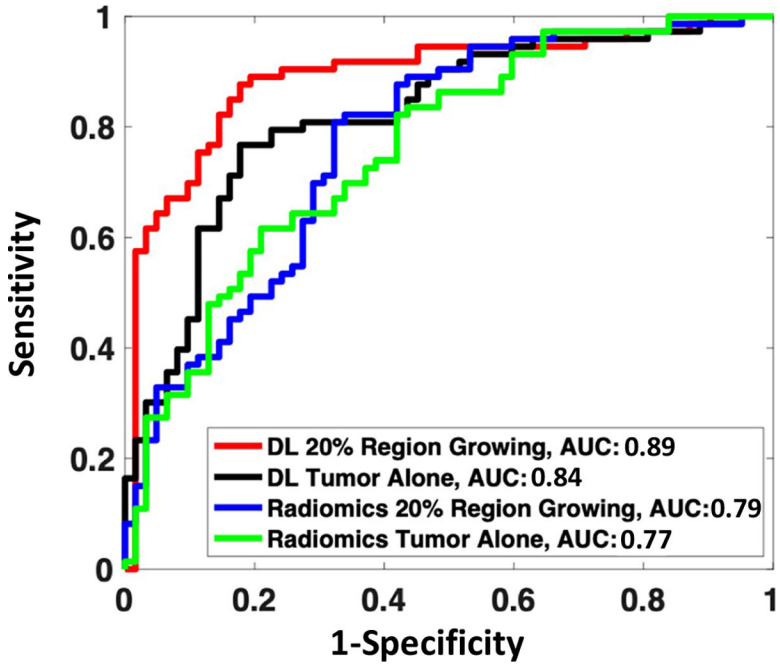

Fig. 12.

The whole group ROC curve constructed by the malignancy probability obtained from the deep learning with the bi-directional CLSTM network and the radiomics analysis. The results of tumor alone and tumor with 20% region growing peritumor tissue are shown, indicating that including some peritumoral tissue can improve the diagnostic performance. Overall, the AUC of deep learning is higher than that of the radiomics analysis for all different ROIs

Table 1

Subject information

		PCa	BPH
		N = 73	*N* = 62
Age (years), median (IQR)		66 (47–81)	65 (47–80)
tPSA (ng/mL), median (IQR)		11.05 (0.02–157)	6.18 (0.48–36)
PI-RADS v2 Score	2	0	62 (100%)
	3	17 (23.3%)	0
	4	21 (28.8%)	0
	5	35 (47.9%)	0
ISUP Grade	1	5 (6.8%)	
	2	24 (32.9%)	
	3	22 (30.1%)	
	4	5 (6.8%)	
	5	17 (23.3%)	

Table 2

ROC results of deep learning and radiomics diagnostic models developed using different ROIs, and the comparison between them by using the DeLong test

	Deep learning		Radiomics		DeLong test	
	AUC range	**Mean AUC**	**AUC range**	**Mean AUC**	***Z* value**	***p* value**
Lesion only-no peritumor	0.72–0.89	0.84	0.70–0.82	0.77	1.34	0.18
Volumetric expansion 1.2 times larger shell	0.71–0.94	0.85	0.71–0.83	0.77	1.55	0.12
1.5 times larger shell	0.64–0.85	0.75	0.62–0.83	0.74	0.17	0.87
Boundary pixel expansion 5 pixels expansion	0.78–0.94	0.87	0.73–0.82	0.78	1.81	0.07
10 pixels expansion	0.76–0.95	0.85	0.70–0.84	0.78	1.37	0.17
15 pixels expansion	0.62–0.87	0.74	0.63–0.77	0.69	0.81	0.42
Region growing expansion ± 20% intensity region growing	0.81–0.93	0.89	0.74–0.85	0.79	2.11	**0.04***
± 30% intensity region growing	0.58–0.86	0.77	0.66–0.75	0.72	0.85	0.4
± 40% intensity region growing	0.57–0.76	0.65	0.51–0.69	0.62	0.45	0.65

Med Biol Eng Comput. Author manuscript; available in PMC 2023 October 04.

Table 3

The DeLong test of the deep learning diagnostic results developed using different ROIs compared to the result of 20% region growing ROI as the reference

	ROC results		Compared to DL model of 20% region growing ROI	
	AUC range	**Mean AUC**	***Z*-value**	***p*-value**
Lesion only-no peritumor	0.72–0.89	0.84	1.14	0.25
Volumetric expansion 1.2 times larger shell	0.71–0.94	0.85	0.93	0.35
1.5 times larger shell	0.64–0.85	0.75	2.8	0.005*
Boundary pixel expansion 5 pixels expansion	0.78–0.94	0.87	0.48	0.63
10 pixels expansion	0.76–0.95	0.85	0.93	0.35
15 pixels expansion	0.62–0.87	0.74	2.97	0.003*
Region growing expansion ± 20% intensity region growing	0.81–0.93	0.89	0	1
± 30% intensity region growing	0.58–0.86	0.77	2.46	0.01*
± 40% intensity region growing	0.57–0.76	0.65	4.4	< 0.001*

*Indicates statistical difference

Table 4

The DeLong test of the radiomics diagnostic results developed using different ROIs compared to the result of 20% region growing ROI as the reference

	ROC results		Compared to radiomics model of 20% region growing ROI	
	AUC range	Mean AUC	Z-value	P-value
Lesion only-no peritumor	0.70–0.82	0.77	0.36	0.72
Volumetric expansion				
1.2 times larger shell	0.71–0.83	0.77	0.36	0.72
1.5 times larger shell	0.62–0.83	0.74	0.88	0.38
Boundary pixel expansion				
5 pixels expansion	0.73–0.82	0.78	0.18	0.86
10 pixels expansion	0.70–0.84	0.78	0.18	0.86
15 pixels expansion	0.63–0.77	0.69	1.69	0.09
Region growing expansion				
± 20% intensity region growing	0.74–0.85	0.79	0	1
± 30% intensity region growing	0.66–0.75	0.72	1.21	0.22
± 40% intensity region growing	0.51–0.69	0.62	2.78	0.006 *

* Indicates significant difference